



## COMPUTATIONAL INVESTIGATION INTO RESISTANCE CHARACTERISTICS OF A PUSHER-BARGE SYSTEM

Ahmad Fitriadhy<sup>1\*</sup>, Nur Amira Adam<sup>2</sup>, Izzati Pison<sup>3</sup>, Mohd Asamudin A. Rahman<sup>4</sup>,  
Mohd Azlan Musa<sup>5</sup> and Mohd Hairil Mohd<sup>6</sup>

<sup>1</sup>Program of Naval Architecture, Faculty of Ocean Engineering Technology and Informatics, Universiti Malaysia Terengganu, 21030 Kuala Terengganu, Terengganu, Malaysia, \*[naoe.afit@gmail.com](mailto:naoe.afit@gmail.com)

<sup>2</sup>Program of Naval Architecture, Faculty of Ocean Engineering Technology and Informatics, Universiti Malaysia Terengganu, 21030 Kuala Terengganu, Terengganu, Malaysia, [amiraadam.nur@gmail.com](mailto:amiraadam.nur@gmail.com)

<sup>3</sup>Undergraduate Student, Faculty of Ocean Engineering Technology and Informatics, Universiti Malaysia Terengganu, 21030 Kuala Terengganu, Terengganu, Malaysia, [nurulizzatipison@gmail.com](mailto:nurulizzatipison@gmail.com)

<sup>4</sup>Faculty of Ocean Engineering Technology and Informatics, Universiti Malaysia Terengganu, 21030 Kuala Terengganu, Terengganu, Malaysia, [mohdasamudin@umt.edu.my](mailto:mohdasamudin@umt.edu.my)

<sup>5</sup>Faculty of Ocean Engineering Technology and Informatics, Universiti Malaysia Terengganu, 21030 Kuala Terengganu, Terengganu, Malaysia, [mohdazlan@umt.edu.my](mailto:mohdazlan@umt.edu.my)

<sup>6</sup>Faculty of Ocean Engineering Technology and Informatics, Universiti Malaysia Terengganu, 21030 Kuala Terengganu, Terengganu, Malaysia, [m.hairil@umt.edu.my](mailto:m.hairil@umt.edu.my)

### Abstract:

*Prediction of the total resistance of a pusher-barge system has become enormous complexity involving nonlinear-hydrodynamic flow behaviour around their hull forms. Both empirical and simplified numerical solutions may still lead to inaccurate results due to the presence of nonlinear characteristics of the pressure and viscous resistances. The use of a more sophisticated method would obviously necessitate solving the above problem. This paper presents a Computational Fluid Dynamics (CFD) approach to predict the total resistance of a pusher-barge system at various barge configurations. To achieve such an objective, four different configurations of the barge models incorporated with various Froude numbers have been taken into account in the computational simulation. In general, the results revealed that the increase of Froude number ( $Fr = 0.182$  to  $0.312$ ) was proportional to the magnitude of  $R_T$ ,  $R_P$ , and  $R_V$ . Regardless of the various Froude number, the pusher-barge system with a 13BP configuration provides the highest resistance compared to the 12BP and 11BP. In addition, the arrangement of barges in the longitudinal (12BP) and lateral (21BP) configurations produced a significant effect with increases in  $R_T$ ,  $R_P$ , and  $R_V$  values of 110%, 167.5%, and 77.6%, respectively. The possible reason for this is that the increase of the total wetted surface area for 21BP has produced a proportionally higher amount of pressure and viscous resistance. Finally, the numerical results were presented and analyzed based on some aspects involving the total resistance and resistance coefficient in terms of pressure and viscous resistance of the pusher-barge system. This analysis provides very valuable information on selecting a proper arrangement of the pusher-barge system, which results in less total resistance.*

**Keywords:** CFD, pusher-barge, total resistance, pressure resistance, viscous resistance, hydrodynamic pressure, resistance coefficients

### 1. Introduction

A pusher-barge system that mainly composed of pusher and barge, is one of the efficient transportation systems particularly for rivers and inland waterway transportations. This transportation system has become more popular in ASEAN countries such as Indonesia, Malaysia and Vietnam due to its simple structure, easy operation, low maintenance cost, and safe navigation as compared to a ship's towing transportation system. However, the prediction of the total resistance of a pusher-barge system has become enormous complexity involving nonlinear-hydrodynamic flows behavior around their hull forms (Sano, Yasukawa, Okuda, and Hamaguchi, 2018). In this respect, the investigation on the resistance characteristics primarily quantifying the magnitude of pressure and viscous resistances of the pusher-barge system due to the influence of the flow and pressure fields is appropriately deserved to be studied.

Several researchers have investigated the ship's resistance performance through theoretical and experimental approaches. Peng (2001) found that a complex geometric configuration of vessel has experience a limitation and very difficult to predict the resistance components using the mathematical approach. Besides, the experimental method has been carried out by Uzun et al. (2017) to determine additional resistance due to the increase the surface roughness. The investigation of interference effect of the resistance components such as wave resistance and viscous resistance in wide range of Froude number are experimentally conducted by Insel and Molland (1992) and Song, Demirel, Atlar, et al. (2020). However, this model test required complex procedure, costly expenditure and time-consuming. In addition, Haase et al. (2012), He et al. (2015), Elkafas et al. (2019) and Song et al. (2020) have applied the numerical simulation approaches that look into attainable outcome with precision. In general, the computational results constitute a fairly good agreement and seem realistic compared with experiments as reported by He et al. (2015) and Fitriadhy et al. (2016). Therefore, Computational Fluid Dynamics approach has become prominent and is now an indispensable part of the ship's resistance at the preliminary stage. The growing capabilities of computers allow to face optimistically a fully hydrodynamic approach to the fluid-body interaction problem towards obtaining a more accurate solution, which is possibly satisfied (Elkafas et al., 2019).

This paper presents a Computational Fluid Dynamics (CFD) simulation to predict the total resistance of a pusher-barge system in calm water. A commercial CFD software, namely NUMECA Fine™/ Marine, was utilized by applying the incompressible unsteady Reynolds-Averaged Navier Stokes equations (RANSE) in which RANSE and continuity equations are discretized by the finite volume method based on Volume of Fluid (VOF) to deal with the non-linear free surface. In addition, the computational domain, with adequate numbers of grid meshes, was carefully determined before simulations. Basically, this is solved by means of a mesh independent study to select the optimal domain discretization. Several parameters such as various Froude numbers at a wide range ( $Fr = 0.182$  to  $0.312$ ) and various arrangements of multiple barges both of longitudinal and lateral configurations of the barges have been taken into account in the computational simulation. The results were clearly discussed with respect to the total resistance characteristics focusing on the pressure and viscous resistances, which were quantified by the magnitude of wave elevation, hydrodynamics pressure and turbulence viscosity.

## 2. Theoretical Background

### 2.1 Governing equations

Here, the main equation use by the CFD regularly is Navier-Stokes equation, which basically includes continuity and momentum equations (Ahmad Fitriadhy, Adam, Mansor, et al., 2020; Sapee, 2015). Basically, two equations in accordance with the law conservation of mass and momentum as clearly expressed in Eqs. (1)-(4). The current CFD simulation is based on the incompressible unsteady RANSE, which employs the volume of fluid (VOF) to solve a free surface model (Ahmad Fitriadhy & Adam, 2020).

### 2.2 Conservation equations

In this paper, ISIS-CFD has been applied to solve the unsteady RANSE in multi-phase continuum. Since the flow is considered as incompressible, the continuity and momentum equations are simplified but the energy equation is no longer been used (Ahmad Fitriadhy, Adam, Quah, Koto, & Mahmuddin, 2020). By considering incompressible flow of viscous fluid under isothermal conditions, the mass and momentum conservation equations can be expressed as:

$$\frac{\partial}{\partial t} \int_V \rho dV + \int_S \rho(\vec{U} - \vec{U}_d) \cdot \vec{n} dS = 0 \quad (1)$$

$$\frac{\partial}{\partial t} \int_V \rho U_i dV + \int_S \rho U_i(\vec{U} - \vec{U}_d) \cdot \vec{n} dS = \int_S (\tau_{ij} l_j - p l_i) \cdot \vec{n} \cdot dS + \int_V \rho g_i dV \quad (2)$$

where  $V$  is the control volume bounded by the closed surface  $S$  with a unit normal vector  $\vec{n}$  that moves at the velocity  $\vec{U}_d$ . While  $\vec{U}$  and  $p$  represent the velocity and pressure field, respectively. Then,  $l$  is the identity matrix,  $\tau_{ij}$  represents the viscous stress tensor components and  $g_i$  as the gravity vector. The Volume of Fluid (VOF) is applied to build the spatial discretization of the transport equations. The viscous free-surface flow is captured using the VOF approach (interface capturing techniques) where requires another solution of transport equation to determine the proportion of fluid in each cell, and this is expressed as:

$$\frac{\partial}{\partial t} \int_V c_i dV + \int_S c_i (\vec{U} - \vec{U}_d) \cdot \vec{n} dS = 0 \tag{3}$$

$c_i$  is the  $i^{th}$  volume fraction for fluid  $i$  and used in between the value 0 and 1 represent a mixture between two fluids. Thus, the value of 0.5 is then selected to indicate the relative proportion of fluid occupying the cell.

### 2.3 Turbulence model

In the current CFD simulation, we propose the SST  $k - \omega$  (SST for shear-stress transport) model, which is available inside ISIS-CFD solver code, where  $k$  is the turbulent kinetic energy and  $\omega$  is the specific dissipation rate. Florianr Menter (1993), and F. R. Menter (1994) reported that the SST  $k - \omega$  model combines several desirable elements of existing two-equation models. Spalart and Allmaras (1992) and Baldwin and Barth (1991) highlighted that the SST  $k - \omega$  model here is set to improve the predictions obtained with algebraic mixing-length models to develop a local model for complex flows, and to provide a simpler alternative for two-equation turbulence models. The two transport equations of the model are defined below with a blending function  $F_1$  for the model coefficients of the original  $\omega$  and  $\varepsilon$  model equations and are written as:

$$\frac{\partial \rho K}{\partial t} + \frac{\partial}{\partial x_j} \left( \rho U_j K - (\mu + \sigma_k \mu_t) \frac{\partial K}{\partial x_j} \right) = \tau_{ij} S_{ij} - \beta^* \rho \omega K \tag{4}$$

$$\frac{\partial \rho \omega}{\partial t} + \frac{\partial}{\partial x_j} \left( \rho U_j \omega - (\mu + \sigma_\omega \mu_t) \frac{\partial \omega}{\partial x_j} \right) = P_\omega - \beta \rho \omega^2 + 2(1 - F_1) \frac{\rho \sigma_{\omega 2}}{\omega} \frac{\partial K}{\partial x_j} \frac{\partial \omega}{\partial x_j} \tag{5}$$

where the last source term of Eq. (6) represents the cross-diffusion term that appears in the transformed  $\omega$ -equation from the original  $\varepsilon$ -equation. Florian Menter and Rumsey (1994) noted that the production term of  $\omega$  is sometimes approximated as proportional to the absolute value vorticity:

$$P_\omega = 2\gamma\rho \left( S_{ij} - \frac{\omega S_{nn} \delta_{ij}}{3} \right) S_{ij} \cong \gamma\rho \Omega^2 \tag{6}$$

The auxiliary blending function  $F_1$ , designed to blend the model coefficient of the original  $k - \omega$  model in boundary layer zones with the transformed  $k - \varepsilon$  model in free-shear layer and free-stream zones, is defined as follows:

$$F_1 = \left\{ \left[ \min \left\{ \max \left\{ \frac{\sqrt{K}}{0.09K\omega}, \frac{500\mu}{\rho d^2 \omega} \right\}, \frac{4\phi\sigma_{\omega 2}k}{CD_{k\omega}d^2} \right\} \right]^4 \right\} \tag{7}$$

where  $CD_{k\omega} = \max \left\{ \frac{2\rho\sigma_{\omega 2}}{\omega} \frac{\partial K}{\partial x_j} \frac{\partial \omega}{\partial x_j}, 10^{-20} \right\}$ . Here,  $CD_{k\omega}$  is the cross-diffusion in the  $k - \omega$  model.

### 2.4 Total Resistance Prediction of a Ship

Referring to resistance theory, the total resistance of a ship can be expressed in Equation (8) as the sum of the frictional resistance ( $R_F$ ) and the pressure resistance ( $R_P$ ).

$$R_T = R_F + R_P \tag{8}$$

where the coefficient of the total resistance is expressed as (Molland, Wellicome, & Couser, 1994):

$$C_T = \frac{R_T}{0.5 \times \rho \times WSA \times V_S^2} \tag{9}$$

where,  $R_T$  is the dimensional total resistance,  $\rho$  is the water density,  $WSA$  is the wetted surface area of the ship at rest and  $V_S$  is the forward speed.

## 3.0 Simulation Condition

### 3.1 Principal data of the ship

The body plans of the pusher-barge system are clearly displayed in Fig. 1. The ship particulars consist of the pusher and barge are completely summarized in Table 1.

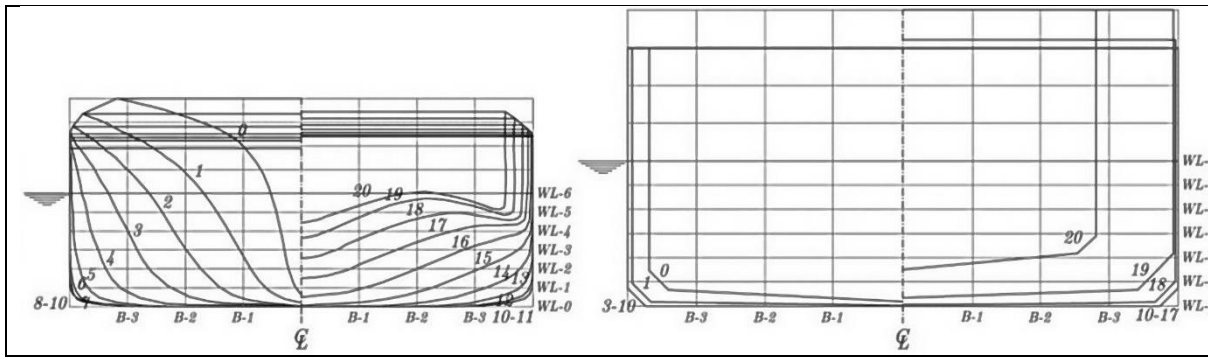


Fig. 1: Body plan of the pusher (left) and the barge (right), King et al. (2008)

Table 1: Principal dimensions of the pusher and barge

| Geometrical Parameter   | Pusher     |             | Barge      |             |
|---|------------|-------------|------------|-------------|
|   | Full scale | Model Scale | Full scale | Model Scale |
| Length between perpendiculars, LBP (m)                                | 40.0       | 0.80        | 60.96      | 1.219       |
| Breadth, B (m)  | 9.0        | 0.18        | 10.67      | 0.213       |
| Draft, d (m)  | 2.2        | 0.044       | 2.74       | 0.055       |
| Longitudinal center of buoyancy (LCB) from aft perpendicular (AP) (m) | 21.98      | 0.440       | 29.44      | 0.589       |
| Block coefficient, $C_B$  | 0.633      |             | 0.924      |             |

### 3.2 Simulation parameter

In the current CFD simulation, several parametric studies such as configurations of the pusher-barge system and Froude numbers have been taken into consideration (see Fig. 2). The details of simulation parameter are completely summarized in Table 2.

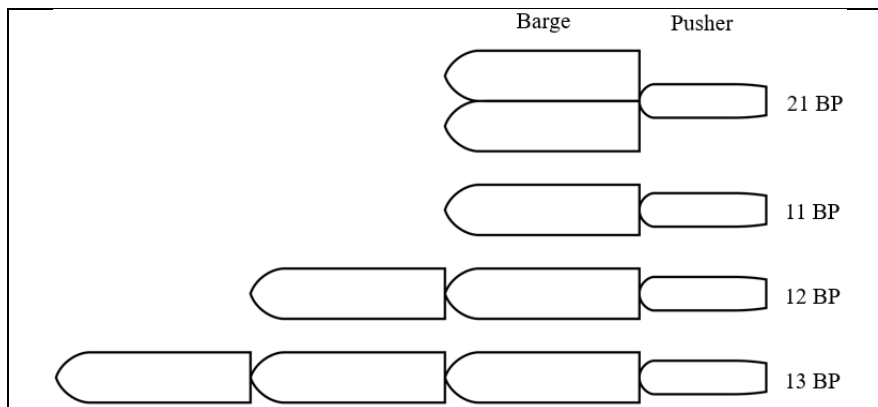


Fig. 2: Simulation conditions of various configurations the pusher-barge system

### 3.3 Computation domain and meshing generation

The computational domain of the pusher-barge model system associated with the unstructured hexahedral meshes is shown in Fig. 3. An extra local refinement of the mesh was added around the free surface to capture the waves that were generated by the pusher ship and barge hull during computation. In addition, the local refinement was employed by surrounding the global meshed computational domain. Corresponding, the maximum number of this

local box refinement was set as the maximum global number of refinements. In this simulation, the local maximum number was determined as equal to 12. Meanwhile, another surface is employed as a triangle, which is purposed to capture the effective area in both x and y directions. Furthermore, the dimension of the domains for this CFD simulation are presented in Table 3. To reduce the computational time, the authors have applied the symmetrical computational domain model (for all simulation conditions).

Table 2: Matrix of Computational Fluid Dynamics

| Fr    | Pusher-Barge System Configurations |      |      |      |
|-------|------------------------------------|------|------|------|
|       | 11BP                               | 12BP | 13BP | 21BP |
| 0.182 | √                                  | √    | √    | √    |
| 0.208 | √                                  | √    | √    | –    |
| 0.234 | √                                  | √    | √    | –    |
| 0.260 | √                                  | √    | √    | –    |
| 0.286 | √                                  | √    | √    | –    |
| 0.312 | √                                  | √    | √    | –    |

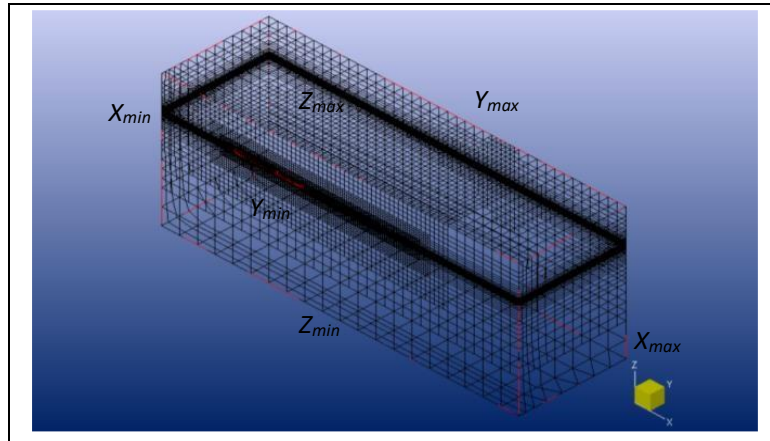


Fig. 3: Mesh generation of pusher-barge system

Referring to Table 3, the external (EXT) boundary type condition was assigned to treat velocity and pressure conditions. Here, the boundary condition for the top and bottom of the patch’s domain were assigned as ‘prescribed pressure’. In this mode, the pressure was imposed during the computation initialization, where the updated hydrostatics pressure was then applied. This means that the pressure is not constantly at 0 (zero) during the computational but it dynamically updates due to the cell mesh moving vertically towards the free surface position. Concerning on the boundary condition for the pusher-barge model, the surfaces were assigned as solid patch.

Table 3: Computational domain and boundary setting

| Description        | Type | Condition           | Length |
|--------------------|------|---------------------|--------|
| $X_{max}$ (Outlet) | EXT  | Far field           | 3L     |
| $X_{min}$ (Inlet)  | EXT  | Far field           | 1L     |
| $Z_{min}$ (Bottom) | EXT  | Prescribed pressure | 1.5L   |
| $Z_{max}$ (Top)    | EXT  | Prescribed pressure | 0.5L   |
| $Y_{min}$ (Side)   | MIR  | Far field           | 1.5L   |
| $Y_{max}$ (Side)   | EXT  | Far field           | 1.5L   |

The meshing generation of the pusher-barge model was created in HEXPRESS 3.1-1 software. It should be noted that an adequate number of mesh is very important to maintain numerical accuracy and steadiness in the computational results regardless of the longer CPU time. Hence, a mesh independent study may need to be performed for each of the three different numbers of cell meshing. Referring to the mesh independent study result, the initial cell meshing of 1,680 was selected in all computed simulation of the pusher-barge model with

reasonable accuracy of the CFD solution (see Table 4). This can be explained by the fact that the increase of initial cell meshing up to 7,680 was unnecessary due to its insignificant influence into the computational result of the total resistance with more computational time, which is not efficient in various test configurations in limited time. Similar to what was applied to the pusher barge of 11BP, we employed the total meshing for the pusher barge configuration of 12BP, 21BP and 13BP are 1,926,539, 2,165,396 and 2,169,354, respectively.

Table 4: Mesh independence study 11BP

| Case     | Number of Division along Cartesian Axis (X, Y, Z) | Total Number of Cell Meshing | Total Resistance, (R <sub>T</sub> ) |
|----------|---|------------------------------|-------------------------------------|
| A        | 20  | 322,107                      | 0.5216                              |
| <b>B</b> | <b>1,680</b>                                      | <b>1,694,726</b>             | <b>0.5078</b>                       |
| C        | 7,680   | 2,496,113                    | 0.5040                              |

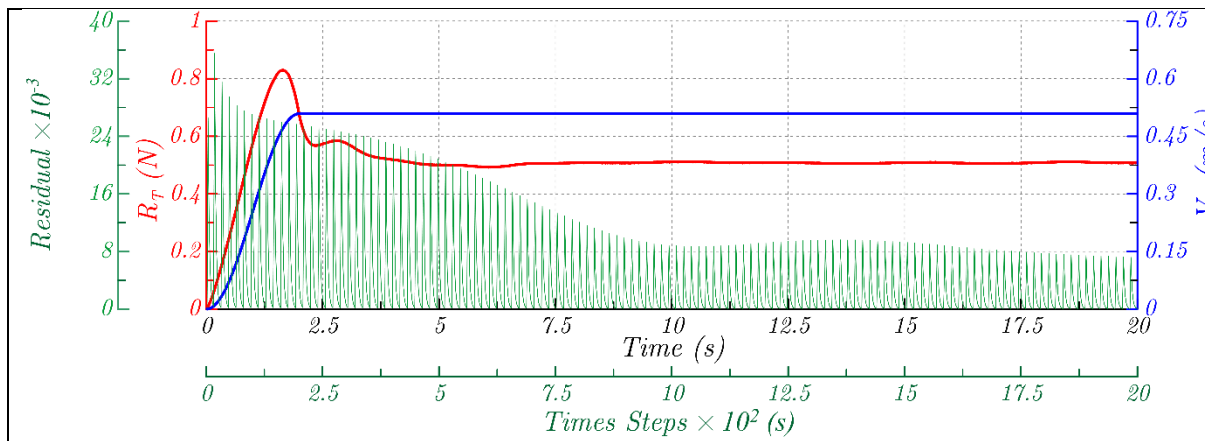


Fig. 4: Time history on the pusher barge system for 11BP using the case ‘B’

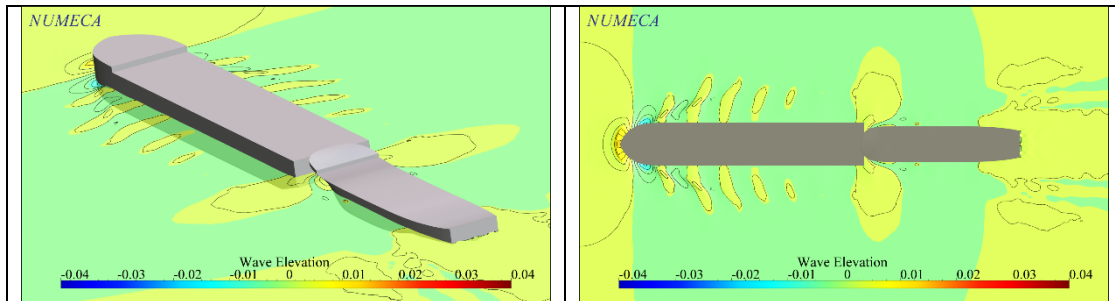


Fig. 5: 3D (left) and 2D (right) of wave pattern and free surface elevation on the pusher barge system for 11BP using the case ‘B’

## 4.0 Results and Discussion

The analysis of resistance and resistance coefficient of the pusher barge system in the effects of various Froude numbers in single and multiple longitudinal configurations and the effects of pusher barge configurations in lateral and longitudinal arrangements have been presented and appropriately discussed in Subsections 4.1 and 4.2, respectively. In this study, the Computational Fluid Dynamics was adopted to obtain the resistance performance of the pusher barge system.

### 4.1 Effects of various froude number (single and multiple longitudinal configurations)

The effect of various Froude numbers on the resistance behavior of 11BP are shown in Fig. 6. The results revealed that the subsequent increase the Froude number from  $Fr = 0.182$  up to  $0.312$  was proportional to the total resistance ( $R_T$ ), pressure resistance ( $R_P$ ), and viscous resistance ( $R_V$ ), which are completely summarized in Table 5. The total resistance ( $R_T$ ) and pressure resistance ( $R_P$ ) have significant increments from  $Fr \geq 0.26$  as compared with viscous

resistance ( $R_V$ ). This occurred due to increasing the wave crest at port and starboard sides of the barge (red color) as displayed in Fig. 7 (A Fitriadhy et al., 2016). In fact, this might generate an asymmetrical high hydrodynamic pressure gradient particularly around the port and starboard sides of the barge subjected to the existence of getting a higher wave crest/elevation, which is directly proportional to the viscous and pressure resistances. Referring to Fig. 6, the increase of  $Fr$  has also generally led to an increase the total resistance coefficient ( $C_T$ ) and pressure resistances coefficient ( $C_P$ ). The reason showed by the fact that the high-pressure gradient (red color) appeared at the pusher's bow regions as showed in Fig. 8. This is due to the effect of the flow pattern around the hull geometry at the highest Froude number (Ahmed, 2011). Meanwhile, the further increase of Froude number from  $Fr = 0.182$  up to 0.312 will uncertainly reduce the viscosity coefficient. In case of highest viscous resistance coefficient ( $C_V$ ), the magnitude of turbulence viscosity increases with red color region appeared at pusher and barge model as displayed in Fig. 9.

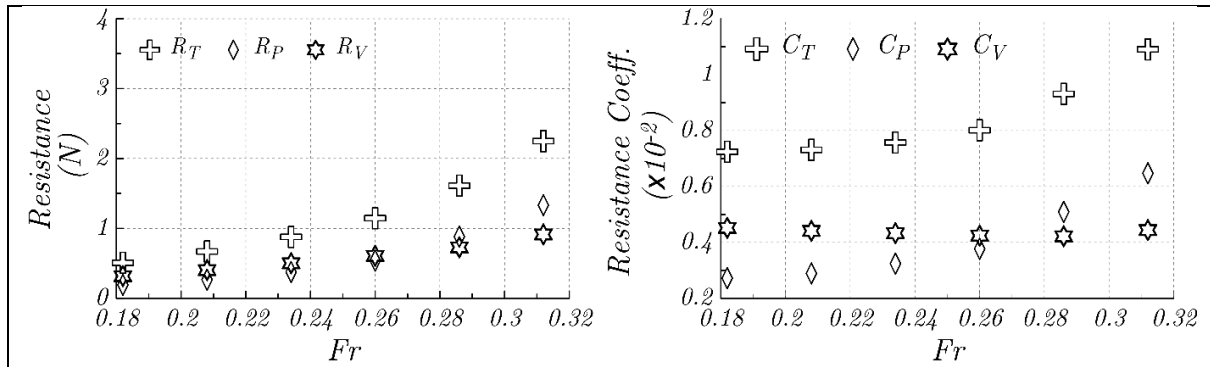


Fig. 6: Resistance (left) and resistance coefficient (right) of 11BP pusher-barge system in various Froude numbers

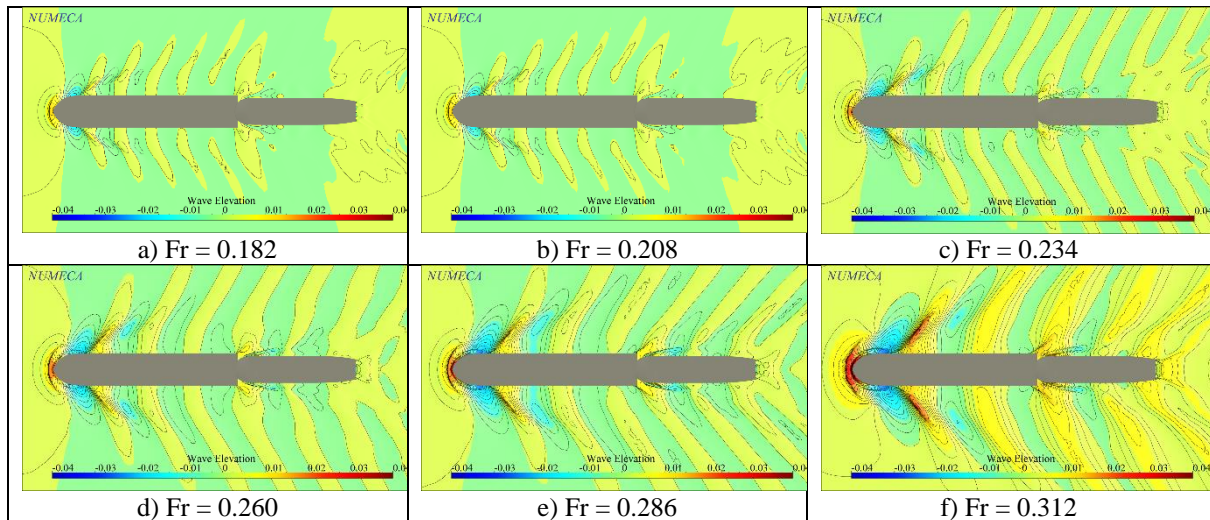


Fig. 7: Characteristics of wave pattern and free surface elevation on pusher barge system at various Froude numbers with 11BP

Table 5: Resistance and resistance coefficient of 11BP pusher-barge system in various Froude numbers.

| Fr    | 11BP      |                            |           |                            |           |                            |
|-------|-----------|----------------------------|-----------|----------------------------|-----------|----------------------------|
|       | $R_T$ (N) | $C_T$ ( $\times 10^{-2}$ ) | $R_P$ (N) | $C_P$ ( $\times 10^{-2}$ ) | $R_V$ (N) | $C_V$ ( $\times 10^{-2}$ ) |
| 0.182 | 0.508     | 0.724                      | 0.191     | 0.272                      | 0.317     | 0.452                      |
| 0.208 | 0.670     | 0.731                      | 0.265     | 0.289                      | 0.404     | 0.441                      |
| 0.234 | 0.878     | 0.757                      | 0.376     | 0.324                      | 0.502     | 0.433                      |
| 0.260 | 1.146     | 0.801                      | 0.539     | 0.377                      | 0.607     | 0.424                      |
| 0.286 | 1.612     | 0.931                      | 0.882     | 0.509                      | 0.730     | 0.422                      |
| 0.312 | 2.248     | 1.090                      | 1.333     | 0.647                      | 0.915     | 0.444                      |

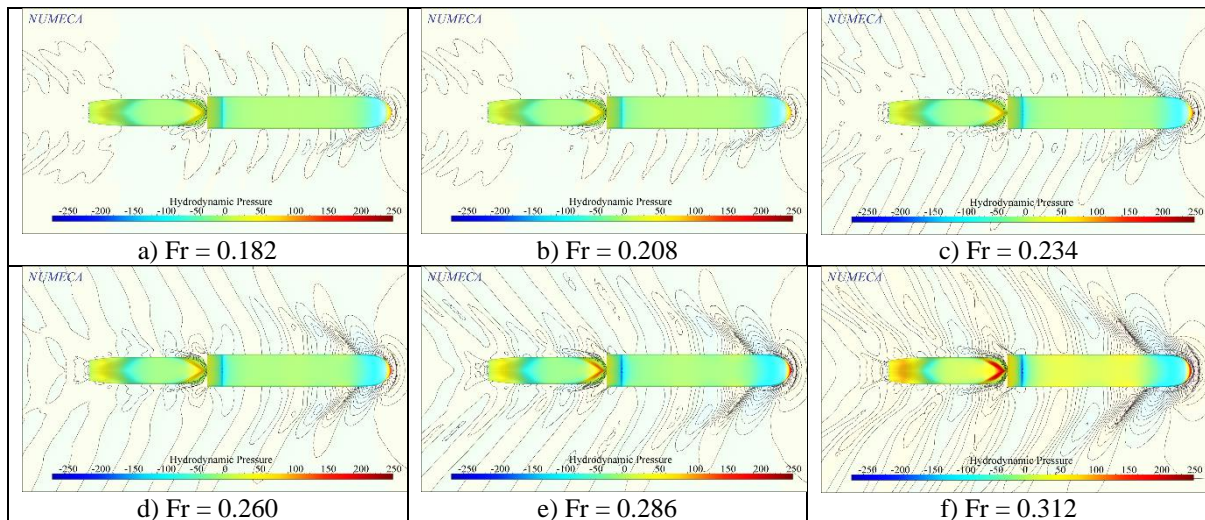


Fig. 8: Hydrodynamic pressure on pusher barge system at various Froude numbers with 11BP

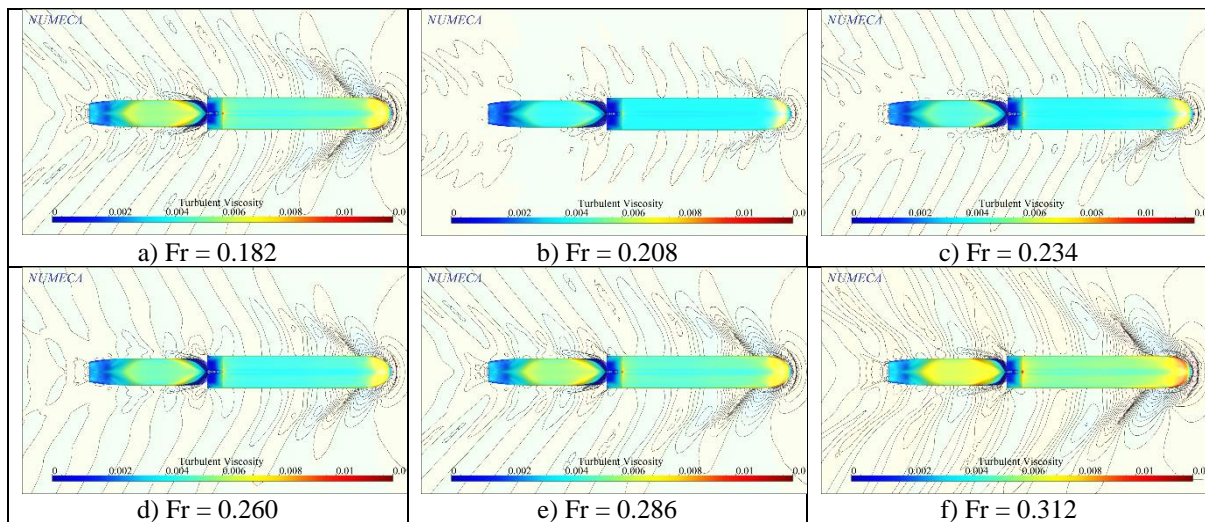


Fig. 9: Turbulent viscosity on pusher barge system at various Froude numbers with 11BP

In addition, the pusher barge system has been also assessed in the multiple longitudinal configurations such as 11BP, 12BP and 13BP, where the results are clearly plotted in Figs. 10~12. The total, pressure and viscous resistances of the multiple configuration of the pusher barge are presented in Table 6~8. The analysis of computed results showed that the subsequent increase of the barge number has resulted in a significant increment of the total resistance ( $R_T$ ), pressure resistance ( $R_P$ ), and viscous resistance ( $R_V$ ), where the longitudinal configuration of 13BP has the highest total resistance. Meanwhile, the highest increments of total resistance ( $R_T$ ), pressure resistance ( $R_P$ ), and viscous resistance ( $R_V$ ) occurred between 11BP to 12BP with 52% ( $Fr = 0.182$ ), 54% ( $Fr = 0.208$ ) and 55.1% ( $Fr = 0.182$ ), respectively. The reason showed by the fact that the hydrodynamic pressure and turbulence viscosity at 13BP indicate by yellow (high hydrodynamics pressure) and blue color (high turbulent viscosity) region reduced significantly at pusher stern (see Figs. 14 and 15), respectively. However, the computational simulations showed that the prediction of resistance coefficient ( $C_T$ ) pressure coefficient ( $C_P$ ) and viscous coefficient ( $C_V$ ) for 11BP, 12BP and 13BP were inversely proportional as increase the barge numbers. The pusher barge system with 11BP configuration produces the highest resistance coefficient as compared with case of 12BP and 13BP configurations. The highest decrements of resistance coefficient ( $C_T$ ), pressure coefficient ( $C_P$ ) and viscous coefficient ( $C_V$ ) occurred between 11BP and 12BP at  $Fr = 0.312$  with 29.3%, 37.7% and 17.1%, respectively. This can be concluded that the increase of number of barges in longitudinal configuration have significant effects to the total resistance and resistance coefficients.

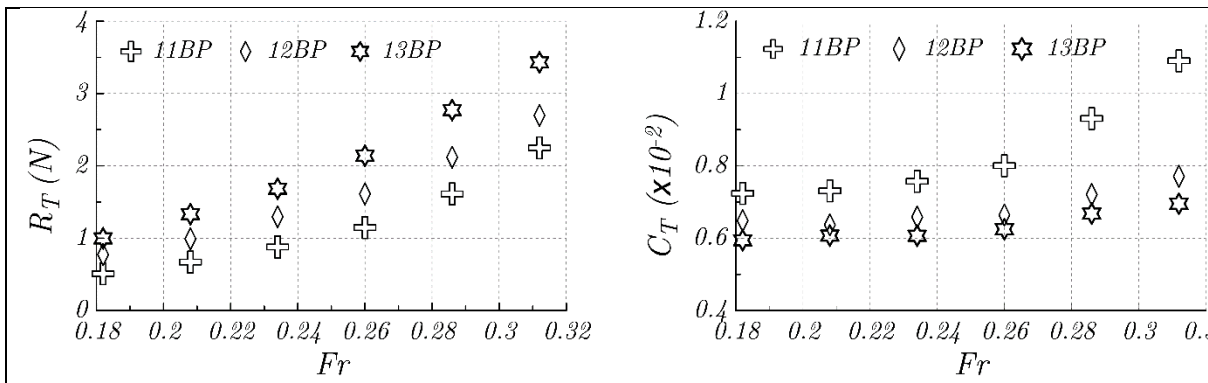


Fig. 10: Total Resistance (left) and resistance coefficient (right) of multiple longitudinal configurations at various Froude numbers

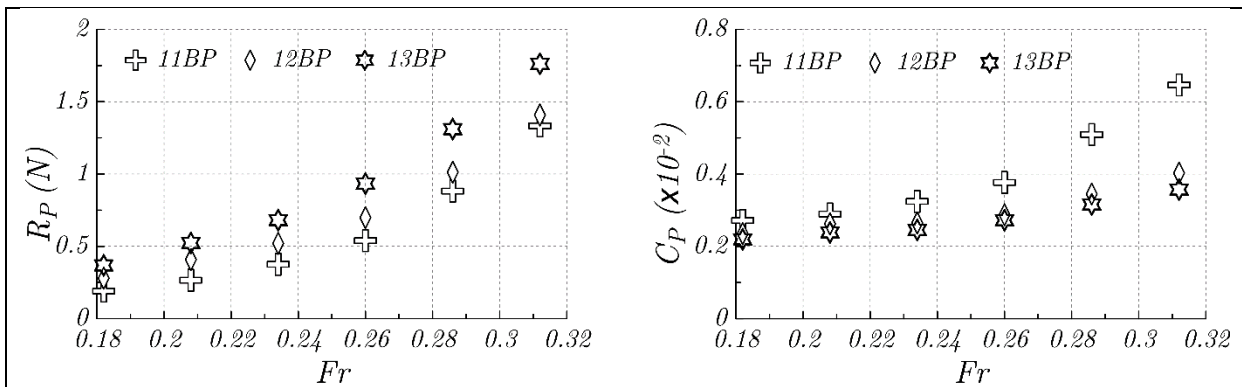


Fig. 11: Pressure Resistance (left) and pressure coefficient (right) of multiple longitudinal configurations at various Froude numbers

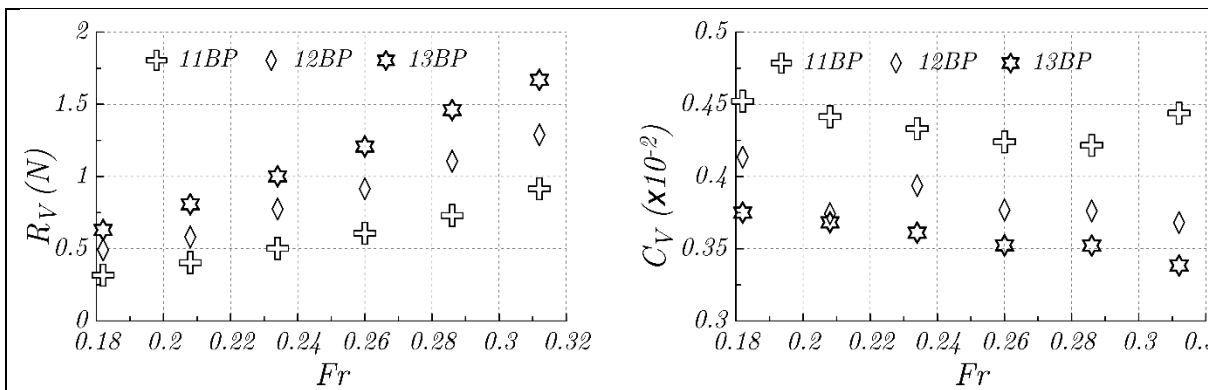


Fig. 12: Viscous Resistance (left) and viscous coefficient (right) of multiple longitudinal configurations at various Froude numbers

Table 6: Total resistance and resistance coefficient of multiple longitudinal configurations in various Froude numbers

| Fr    | 11BP               |                                     | 12BP               |                                     | 13BP               |                                     |
|-------|--------------------|-------------------------------------|--------------------|-------------------------------------|--------------------|-------------------------------------|
|       | R <sub>T</sub> (N) | C <sub>T</sub> (x10 <sup>-2</sup> ) | R <sub>T</sub> (N) | C <sub>T</sub> (x10 <sup>-2</sup> ) | R <sub>T</sub> (N) | C <sub>T</sub> (x10 <sup>-2</sup> ) |
| 0.182 | 0.508              | 0.724                               | 0.772              | 0.648                               | 0.998              | 0.595                               |
| 0.208 | 0.670              | 0.731                               | 0.990              | 0.637                               | 1.332              | 0.607                               |
| 0.234 | 0.878              | 0.757                               | 1.296              | 0.658                               | 1.684              | 0.607                               |
| 0.260 | 1.146              | 0.801                               | 1.613              | 0.664                               | 2.141              | 0.625                               |
| 0.286 | 1.612              | 0.931                               | 2.119              | 0.721                               | 2.770              | 0.668                               |
| 0.312 | 2.248              | 1.090                               | 2.696              | 0.771                               | 3.431              | 0.695                               |

Table 7: Pressure resistance and pressure coefficient of multiple longitudinal configurations in various Froude numbers.

| Fr    | 11BP               |                                     | 12BP               |                                     | 13BP               |                                     |
|-------|--------------------|-------------------------------------|--------------------|-------------------------------------|--------------------|-------------------------------------|
|       | R <sub>P</sub> (N) | C <sub>P</sub> (x10 <sup>-2</sup> ) | R <sub>P</sub> (N) | C <sub>P</sub> (x10 <sup>-2</sup> ) | R <sub>P</sub> (N) | C <sub>P</sub> (x10 <sup>-2</sup> ) |
| 0.182 | 0.191              | 0.272                               | 0.280              | 0.235                               | 0.369              | 0.220                               |
| 0.208 | 0.265              | 0.289                               | 0.408              | 0.263                               | 0.524              | 0.239                               |
| 0.234 | 0.376              | 0.324                               | 0.521              | 0.265                               | 0.682              | 0.246                               |
| 0.260 | 0.539              | 0.377                               | 0.698              | 0.287                               | 0.934              | 0.273                               |
| 0.286 | 0.882              | 0.509                               | 1.013              | 0.345                               | 1.310              | 0.316                               |
| 0.312 | 1.333              | 0.647                               | 1.409              | 0.403                               | 1.761              | 0.357                               |

Table 8: Viscous resistance and viscous coefficient of multiple longitudinal configurations in various Froude numbers.

| Fr    | 11BP               |                                     | 12BP               |                                     | 13BP               |                                     |
|-------|--------------------|-------------------------------------|--------------------|-------------------------------------|--------------------|-------------------------------------|
|       | R <sub>V</sub> (N) | C <sub>V</sub> (x10 <sup>-2</sup> ) | R <sub>V</sub> (N) | C <sub>V</sub> (x10 <sup>-2</sup> ) | R <sub>V</sub> (N) | C <sub>V</sub> (x10 <sup>-2</sup> ) |
| 0.182 | 0.317              | 0.452                               | 0.492              | 0.413                               | 0.630              | 0.375                               |
| 0.208 | 0.404              | 0.441                               | 0.582              | 0.374                               | 0.808              | 0.368                               |
| 0.234 | 0.502              | 0.433                               | 0.775              | 0.394                               | 1.002              | 0.361                               |
| 0.260 | 0.607              | 0.424                               | 0.915              | 0.377                               | 1.208              | 0.352                               |
| 0.286 | 0.730              | 0.422                               | 1.106              | 0.376                               | 1.460              | 0.352                               |
| 0.312 | 0.915              | 0.444                               | 1.288              | 0.368                               | 1.670              | 0.338                               |

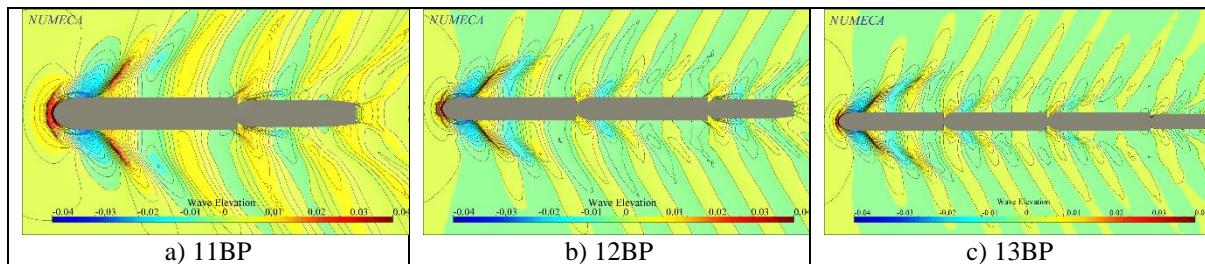


Fig. 13: Characteristics of wave pattern and free surface elevation on multiple longitudinal configurations at Fr = 0.312

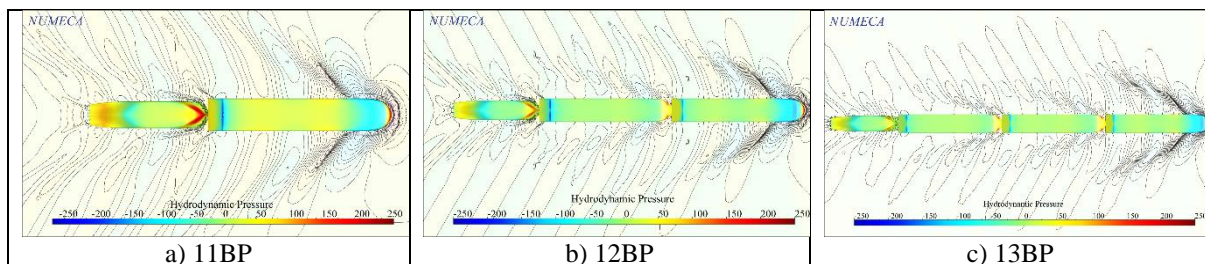


Fig. 14: Hydrodynamics Pressure on multiple longitudinal configurations at Fr = 0.312

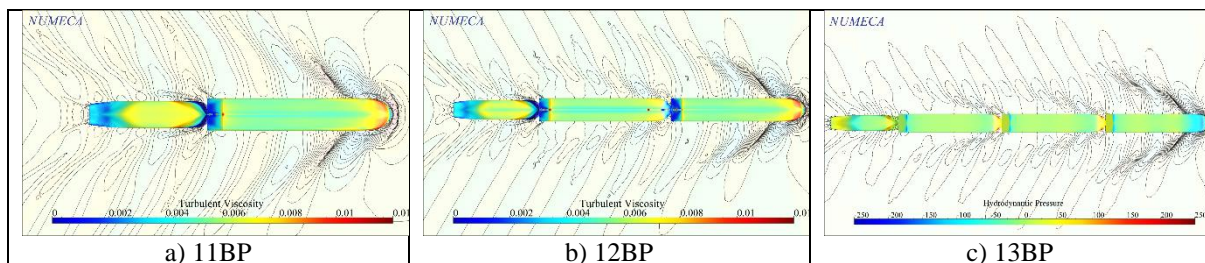


Fig. 15: Turbulent viscosity on multiple longitudinal configurations at Fr = 0.312

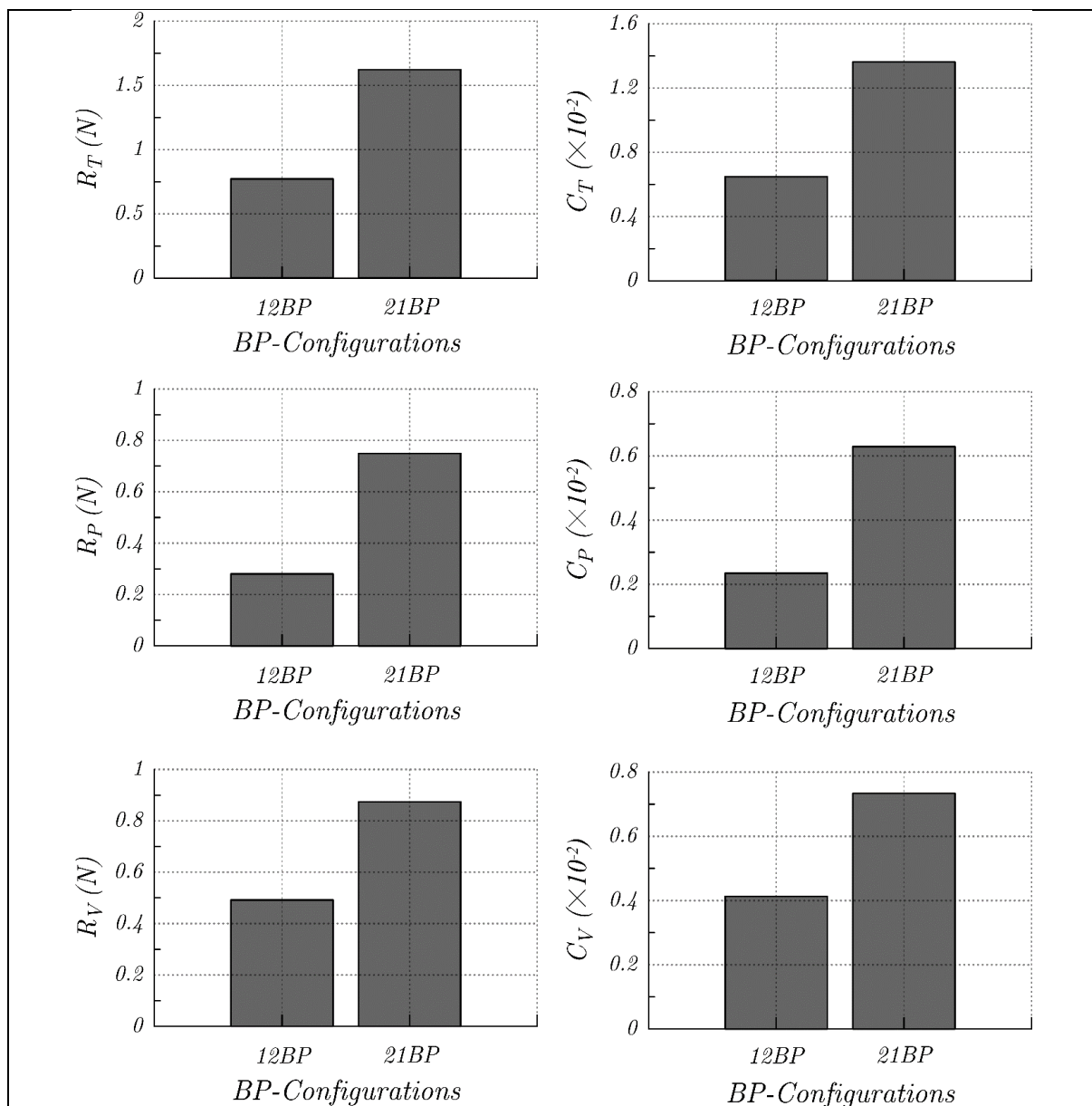


Fig. 16: Resistance (left) and resistance coefficient (right) of longitudinal (left) and lateral (right) arrangements at  $Fr = 0.182$

#### 4.2 Effects of the pusher barge configurations (longitudinal and lateral arrangements)

Fig. 16 shows the total resistance and resistance coefficient characteristics of the pusher barge system in longitudinal (12BP) and lateral (21BP) arrangements. The magnitude of the total resistance and resistance coefficient are completely presented in Table 10. In general, the CFD results revealed that the total resistance and resistance coefficient shows a significant increment between the longitudinal and lateral arrangements of the barge. This can be explained by the fact that the wave elevation indicated by yellow colour region at 21BP configuration increase around the pusher boat as displayed in Fig. 17. It should be noted here that the increments of total resistance ( $R_T$ ), pressure resistance ( $R_P$ ), and viscous resistance ( $R_V$ ) occurred between 12BP to 21BP were 110%, 167.5% and 77.6%, respectively. Meanwhile, the increments of resistance coefficient ( $C_T$ ) Pressure coefficient ( $C_P$ ) and viscous coefficient ( $C_V$ ) occurred between 12BP to 21BP were almost similar with total resistance. These phenomena clearly displayed in Figs. 18 and 19, where the yellow and colour on the configuration of 21BP indicated the increase of the hydrodynamics pressure and turbulent viscosity region,

respectively. Similar to what was explained by King, Yasukawa, Hirata, and Kose (2008), employing of the lateral configuration of the pusher-barge system has required a large powering as compared to the longitudinal ones.

Table 10: Total Resistance and resistance coefficient of pusher barge system in various pusher-barge configurations

| Configurations | $R_T$ (N) | $C_T$ ( $\times 10^{-2}$ ) | $R_P$ (N) | $C_P$ ( $\times 10^{-2}$ ) | $R_V$ (N) | $C_V$ ( $\times 10^{-2}$ ) |
|----------------|-----------|----------------------------|-----------|----------------------------|-----------|----------------------------|
| 12BP           | 0.772     | 0.648                      | 0.280     | 0.235                      | 0.492     | 0.413                      |
| 21BP           | 1.622     | 1.363                      | 0.749     | 0.629                      | 0.874     | 0.734                      |

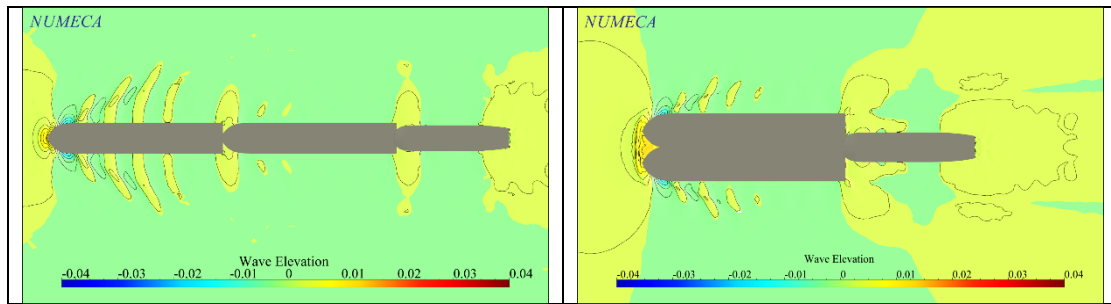


Fig. 17: Characteristics of wave pattern and free surface elevation on longitudinal (left) and lateral (right) arrangements at  $Fr = 0.182$

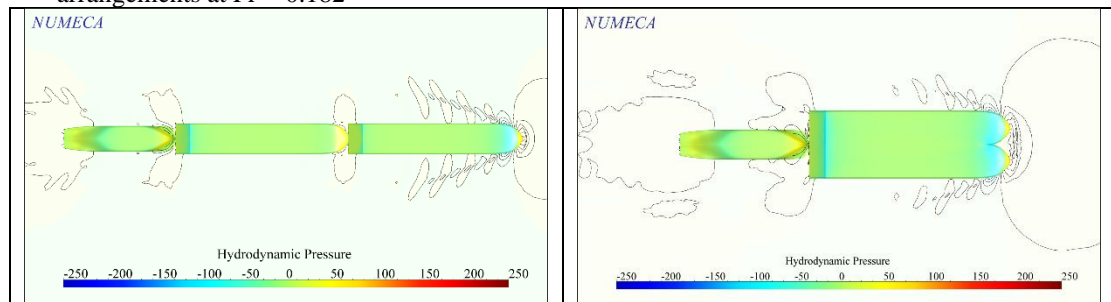


Fig. 18: Hydrodynamics Pressure on longitudinal (left) and lateral (right) arrangements at  $Fr = 0.182$

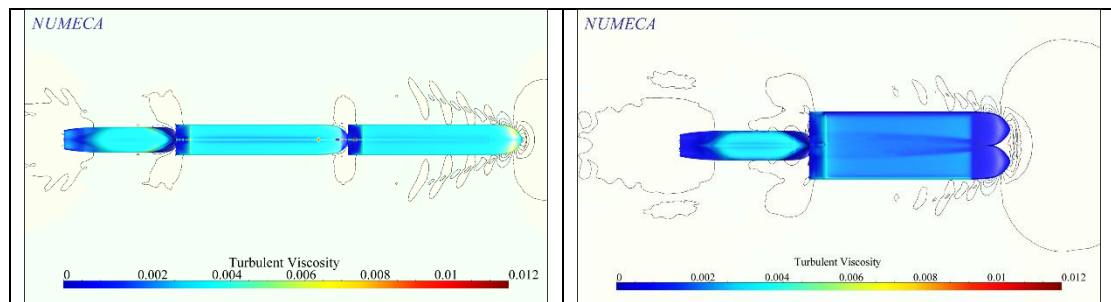


Fig. 19: Turbulent viscosity on longitudinal (left) and lateral (right) arrangements at  $Fr = 0.182$

## 5.0 Conclusions

A simulation of the pusher barge system has been successfully conducted using the computational fluid dynamics. Several parameters such as Froude numbers and pusher barge configuration/arrangements have been considered. The computational results are drawn as follow:

- The subsequent increase of Froude number ( $0.182 \leq Fr \leq 0.312$ ) has significant influence on the resistance and resistance coefficient of the 11BP pusher-barge system. Even so, the viscous coefficient has insignificant reduction as increase the  $Fr$ .
- Regardless of the Froude number, the results showed that the 13BP configuration has achieved the highest resistance. Meanwhile, the highest magnitude of resistance coefficient has been generated at 11BP configuration as compared to others.

- The pusher–barge systems with the same number of barges but arranged in a lateral (21BP) required more power to operate compared to those with barges arranged in longitudinal (12BP).

In addition to this CFD simulation, these results are very useful as preliminary data for the ship resistance, which is primarily required to accurately predict the ship's powering.

## Acknowledgement

This research was not funded by any grant.

## References

- Ahmed, Y. M. (2011). Numerical simulation for the free surface flow around a complex ship hull form at different Froude numbers. *Alexandria Engineering Journal*, 50(3), 229-235.
- Baldwin, B., & Barth, T. (1991). A one-equation turbulence transport model for high Reynolds number wall-bounded flows. Paper presented at the 29th aerospace sciences meeting.
- Elkafas, A. G., Elgohary, M. M., & Zeid, A. E. (2019). Numerical study on the hydrodynamic drag force of a container ship model. *Alexandria Engineering Journal*, 58(3), 849-859.  
<https://doi.org/10.1016/j.aej.2019.07.004>
- Fitriadhy, A., & Adam, A. (2020). CFD analysis on vertical motion of a full-scale floating jetty. *Journal of Sustainability Science and Management*, 15(6), 100-110.  
<https://doi.org/10.46754/jssm.2020.08.009>
- Fitriadhy, A., Adam, N. A., Mansor, N. A., Ahmad, M. F., Jusoh, A., Mokhtar, N. H., & Sulaiman, M. S. (2020). CFD Investigation into the effect of heave plate on vertical motion responses of a floating jetty. *CFD Letters*, 12(5), 24-35.  
<https://doi.org/10.37934/cfdl.12.5.2435>
- Fitriadhy, A., Adam, N. A., Quah, C., Koto, J., & Mahmuddin, F. (2020). CFD prediction of B-series propeller performance in open water. *CFD Letters*, 12(2), 58-68.
- Fitriadhy, A., Lim, P., & Jamaluddin, A. (2016). CFD Investigation on total resistance coefficient of symmetrical and staggered catamaran configurations through quantifying existence of an interference factor. Paper presented at the International Conference on Ships and Offshore Structures. Hamburg, Germany.
- Haase, M., Binns, J., Thomas, G., & Bose, N. (2012). Resistance prediction of medium-speed catamarans using free-surface viscous flow simulations. Paper presented at the 15th Numerical Towing Tank Symposium.
- He, W., Castiglione, T., Kandasamy, M., & Stern, F. (2015). Numerical analysis of the interference effects on resistance, sinkage and trim of a fast catamaran. *Journal of marine science and technology*, 20(2), 292-308.  
<https://doi.org/10.1007/s00773-014-0283-0>
- Insel, M., & Molland, A. (1992). An investigation into the resistance components of high speed displacement catamarans.
- King, K. K., Yasukawa, H., Hirata, N., & Kose, K. (2008). Maneuvering simulations of pusher-barge systems. *Journal of marine science and technology*, 13(2), 117-126.
- Menter, F. (1993). Zonal two equation kw turbulence models for aerodynamic flows. Paper presented at the 23rd fluid dynamics, plasmadynamics, and lasers conference.
- Menter, F., & Rumsey, C. (1994). Assessment of two-equation turbulence models for transonic flows. Paper presented at the Fluid Dynamics Conference.
- Menter, F. R. (1994). Two-equation eddy-viscosity turbulence models for engineering applications. *AIAA journal*, 32(8), 1598-1605.
- Molland, A., Wellicome, J., & Couser, P. (1994). Resistance experiments on a systematic series of high speed displacement catamaran forms: variation of length-displacement ratio and breadth-draught ratio.
- Peng, H. (2001). Numerical computation of multi-hull ship resistance and motion.
- Sano, M., Yasukawa, H., Okuda, A., & Hamaguchi, T. (2018). Maneuverability of a pusher and barge system under empty and full load conditions. *Journal of Marine Science and Technology*, 23(3), 464-482.  
<https://doi.org/10.1007/s00773-017-0485-3>
- Sapee, S. (2015). Computational fluid dynamics study on droplet size of kerosene fuel. *Journal of Advanced Research in Fluid Mechanics and Thermal Sciences*, 16(1), 1-14.
- Song, S., Demirel, Y. K., Atlar, M., Dai, S., Day, S., & Turan, O. (2020). Validation of the CFD approach for modelling roughness effect on ship resistance. *Ocean Engineering*, 200, 107029.  
<https://doi.org/10.1016/j.oceaneng.2020.107029>

Song, S., Demirel, Y. K., Muscat-Fenech, C. D. M., Tezdogan, T., & Atlar, M. (2020). Fouling effect on the resistance of different ship types. *Ocean Engineering*, 216, 107736.

<https://doi.org/10.1016/j.oceaneng.2020.107736>

Spalart, P., & Allmaras, S. (1992). A one-equation turbulence model for aerodynamic flows. Paper presented at the 30th aerospace sciences meeting and exhibit.

Uzun, D., Zhang, Y., Demirel, Y. K., & Turan, O. (2017). Experimental determination of added resistance due to barnacle fouling on ships by using 3D printed barnacles.